High-resolution frequency-comb spectroscopy with electro-optic sampling and instantaneous octave-wide coverage across mid-IR to THz at a video rate

Cite as: APL Photon. 8, 110801 (2023); doi: 10.1063/5.0165879
Submitted: 30 June 2023 • Accepted: 12 October 2023 •
Published Online: 6 November 2023

Dmitrii Konnov,[1] Andrey Muraviev,[1] Sergey Vasilyev,[2] and Konstantin Vodopyanov[1,a)]

AFFILIATIONS

[1] CREOL, College of Optics and Photonics, University of Central Florida, Orlando, Florida 32816, USA
[2] IPG Photonics Corporation, 377 Simarano Drive, Marlborough, Massachusetts 01752, USA

Note: This paper is part of the APL Photonics Special Topic on State-of-the-Art and Future Directions in Optical Frequency Comb Sources, Enabling Technologies, and Applications.
[a)]**Author to whom correspondence should be addressed:** vodopyanov@creol.ucf.edu

ABSTRACT

Ultrabroadband electro-optic sampling using few-optical-cycle probing pulses is a sensitive technique to detect electric field amplitudes with a high dynamic range and up to near-infrared optical frequencies. By combining this method with dual-frequency-comb spectroscopy and using a new class of ultrafast lasers, we perform high-resolution, 80 MHz/0.0027 cm^{-1} (10 MHz/0.0003 cm^{-1} with spectral interleaving), spectroscopic measurements in the frequency range 1.5–45 THz (6.6–200 μm), excluding the strongly absorbing Reststrahlen band of lattice resonances at 4.5–9 THz, with an instantaneous spectral coverage exceeding an octave (e.g., 9–22 μm). As a driving source, we use a pair of mutually coherent combs from Kerr-lens mode-locked solid-state Cr:ZnS (2.35 μm) lasers. One of the combs is frequency downconverted via intrapulse difference frequency generation to produce a longwave "sensing" comb, while the second comb is frequency doubled to produce a near-IR "probe" comb for electro-optic sampling (EOS). The low intensity and phase noise of our dual-comb system allow for capturing a large amount of spectral information (200 000 comb-mode-resolved spectral lines spaced by 80 MHz) in the mid-IR portion of the spectrum at a video rate of 69 Hz, with the signal-to-noise ratio limited by the shot noise of the near-IR EOS balanced detection system. Our dual-comb spectroscopy measurements with low-pressure gaseous ethanol, isoprene, and dimethyl sulfide reveal Doppler-limited spectroscopic signatures that have never been explored before.

I. INTRODUCTION

The technique of dual-comb spectroscopy (DCS)[1,2] has been rapidly expanding over the last two decades, starting with the proof-of-concept work[3] where the key advantages of this method over the traditional Fourier transform infrared spectrometry were revealed, namely broadband coverage combined with high spectral resolution, high acquisition speed, high precision, and the absence of moving parts. The mid-infrared (MIR) to THz spectral region is of special interest for molecular spectroscopy and trace molecular detection since molecules have their strongest absorption bands across this range. Significant progress in generating broadband MIR frequency combs became possible due to the new development of mode-locked fiber[4] and solid-state[5–8] lasers and the efficient downconverting of their frequencies through optical parametric oscillation (OPO),[9–12] difference-frequency generation (DFG),[13,14] and intra-pulse DFG (IDFG)[15,16] based on advanced $\chi^{(2)}$ nonlinear crystals.[17–19] Simultaneously, great effort has been made in developing chip-scale frequency combs based on microresonators and waveguides,[20–23] quantum cascade lasers,[24–26] interband cascade lasers,[27] and electro-optic modulators.[14,28]

Recently, a system has been reported that for the first time has simultaneously demonstrated all of the advantages of the dual-comb method, namely: (i) broadband instantaneous spectral coverage

(6.6–11.4 μm), (ii) superior resolution (80 MHz/0.0027 cm^{-1}), and (iii) high detection speed (10 Hz) based on efficient downconversion of 2.35-μm combs to the longwave IR (LWIR) domain via IDFG in zinc germanium phosphide (ZGP) crystals and acquisition of interferograms using a HgCdTe (T = 77 K) photodetector.[28] However, reaching longer, >12 μm wavelengths remains a major challenge for photon detectors, as they suffer from higher noise and slower response, even when operating at cryogenic temperatures.

Kowligy *et al.*[29] pioneered a new approach to DCS that combines the IDFG method to create a LWIR sensing comb and to electro-optically detect using a near-infrared (NIR) probe comb, eliminating the need for LWIR photodetectors. Essentially, electro-optic sampling (EOS) combines three advanced techniques for low-noise detection of LWIR radiation: (i) up-conversion to NIR frequencies; (ii) optical time gating that eliminates background noise; and (iii) heterodyning that allows, in theory, quantum-limited LWIR detection.[30–32]

Here, we report a novel approach to EOS-DCS based on mode-locked Cr:ZnS 2.35-μm lasers as the driving source. These lasers have emerged as longwave alternatives to Ti:Sapphire technology, offering several benefits including efficient laser pumping schemes and high laser to LWIR downconversion efficiency; this enables conducting spectroscopic measurements over the frequency range of 1.5–45 THz (wavelength range 6.6–200 μm), excluding around 4.5–9 THz due to the Reststrahlen band of the nonlinear material used, and measurements in this range taken with instantaneous octave-spanning spectral coverage, absolute frequency referencing, and the capability of resolving up to 200 000 comb-mode lines at a video rate.

II. EXPERIMENTAL SETUP

A. Driving laser combs at 2.35 μm

The front end of our system is a pair of phase locked laser frequency combs (Fig. 1, inset), each consisting of a polycrystalline Kerr-lens mode-locked Cr:ZnS master oscillator and a single-pass Cr:ZnS power amplifier, both pumped by Er-doped fiber lasers at 1567 nm.[6,7] The system operates at a repetition rate $f_{rep} \approx 80$ MHz, a central wavelength of 2.35 μm, and a full-width half-maximum (FWHM) bandwidth of 280 nm. Depending on the amplifier pump power, the average output power varies from 0.86 to 3.15 W, with the pulse duration varying, respectively, from 33 to 25 fs.

To stabilize the carrier envelope offset frequency (f_{ceo}) of both combs, about 20% of each oscillator power is deflected with a beam splitter and focused into a periodically poled lithium niobate (PPLN) crystal (Fig. 1, inset). A custom-designed PPLN with three sections of different quasi-phase-matching periods generates second, third, and fourth harmonics that are used for f_{ceo} detection via 3f-to-4f nonlinear interferometry at wavelengths of 600–650 nm. For the optical referencing, we utilize the second harmonic parasitically produced (via random phase matching) in the oscillator Cr:ZnS polycrystal, which is transmitted through one of the dichroic mirrors of the oscillator cavity and heterodyned with a stable ultra-narrow linewidth 1064-nm continuous-wave (CW) reference laser (common for both Cr:ZnS combs) that produces the beat frequency f_{opt}.

The error signal between the f_{ceo} beat and a synthesized reference signal is fed into a feedback loop that controls f_{ceo} through changing the oscillator pump power, while the error signal between f_{opt} and another synthesized reference is fed into a feedback loop to control the oscillator cavity length with a piezo transducer. Both synthesized radiofrequency signals are referenced to an Rb atomic clock.

The integrated (10 Hz–10 MHz) phase noise of the f_{ceo} and f_{opt} signals was <0.05 and <0.1 rad, respectively, which indicates robust phase locking. We consider the mutual coherence time between the two combs to be at least 100 s,[28] and the absolute position of each comb tooth is given by the Rb clock accuracy (10^{-10}).

B. MIR to THz combs produced by intrapulse difference frequency generation

Producing broadband transients via intra-pulse difference-frequency generation (IDFG) in $\chi^{(2)}$ crystals using few-optical-cycle pulses is a simple yet powerful technique for generating offset-free

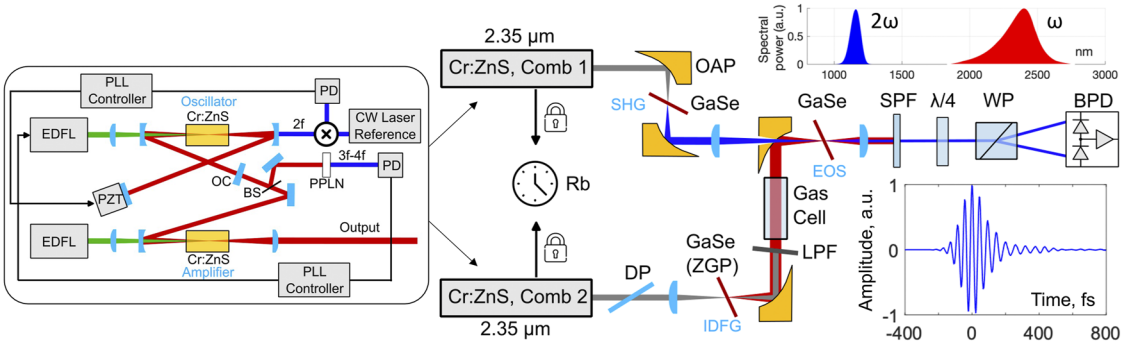

FIG. 1. Schematic of the EOS DCS spectroscopy setup. The inset (left) shows the Cr:ZnS laser system and its stabilization arrangement. The inset (top right) shows the normalized spectra of the fundamental (ω) Cr:ZnS laser output along with its second harmonic (2ω). The inset (bottom right) shows the central portion of the field-resolved MIR waveform. EDFL, Er-doped fiber laser; PLL, phase-locked loop; PZT, piezo transducer; OC, output coupler; BS, beam splitter; PD, InGaAs detector for f_{opt} detection; and Si avalanche photodetector for 3f-to-4f interferometry; Rb, Rubidium atomic clock; DP, dispersive plate; OAP, off-axis parabolic mirror; LPF, longpass filter; SPF, shortpass filter; λ/4, quarter-wave plate; WP, Wollaston prism; BPD, InGaAs balanced photodetector.

combs in the MIR/THz regions.[31] Depending on the spectral range, we performed IDFG using two nonlinear crystals: $ZnGeP_2$ (ZGP) and GaSe. The ZGP crystal allows the generation of MIR transients with a conversion efficiency exceeding 10% (thanks to its high nonlinearity and excellent group-velocity matching between the 2.35-μm pump and MIR output[16]). While in ZGP, the output spectral power declines at $\lambda > 12.5$ μm due to two-phonon resonances, GaSe can produce outputs spanning beyond 20 μm, albeit at a lower output power.

In the case of ZGP, the driving laser beam is pre-chirped with a 2-mm-thick sapphire and 1-mm YAG plates (both having the opposite sign of the group velocity dispersion with respect to ZGP) and focused into a 3 mm thick antireflection (AR) coated ZGP using a f = 75 mm CaF_2 lens. The ZGP crystal is cut for type I phase matching with polar and azimuthal angles of $\theta \approx 50^\circ$ and $\phi \approx 0^\circ$; its orientation (as seen from the incoming beam) is shown in Fig. 2(a). Since the IDFG phase matching in ZGP requires pump waves with two orthogonal polarizations, "e" and "o," corresponding to the process $\omega_3^0 - \omega_2^e = \omega_1^e$ (where $\omega_3 > \omega_2 > \omega_1$, ω_3 and ω_2 are the two frequency components of the same broadband pump, and ω_1 is the longwave output frequency), the crystal is placed in such a way that its "e" and "o" polarization directions are at 45° with respect to the input laser polarization,[16] horizontal in the laboratory frame [Fig. 2(a)]. Figure 2(d) shows the calculated 2D color-coded plot for the normalized IDFG output E-field amplitude in ZGP that takes into account (i) the phase-matching function $sinc(\Delta kL/2)$ and (ii) frequency-dependent conversion efficiency accounting for the finite spectral band of the pump laser as a function of the output frequency and phase-matching angle θ. (It does not account for the longwave absorption in the crystal.) Here, Δk is the k-vector mismatch and L is the length of the crystal.

The generated IDFG beam (its polarization direction, "e"-wave relative to ZGP, is at −45° with respect to the vertical axis of the laboratory system) was collimated with an off-axis parabolic mirror (OAP). With 2.8 W of driving laser power, the IDFG output power reached 300 mW after a longpass filter (LPF, $\lambda > 6.7$ μm) with a typical spectrum shown in Fig. 3(a).

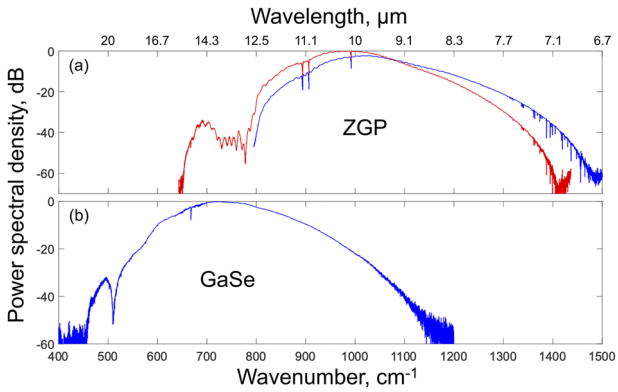

FIG. 3. Typical IDFG output spectra measured with EOS. (a) Obtained in a 3-mm ZGP after a 6.7-μm long-pass filter (LPF) for two different phase-matching angles of the EOS crystal. (b) Obtained in 1.3-mm GaSe after 7.4-μm LPF. The longwave part of the spectrum (<500 cm^{-1}) was attenuated by the germanium windows of the gas cell.

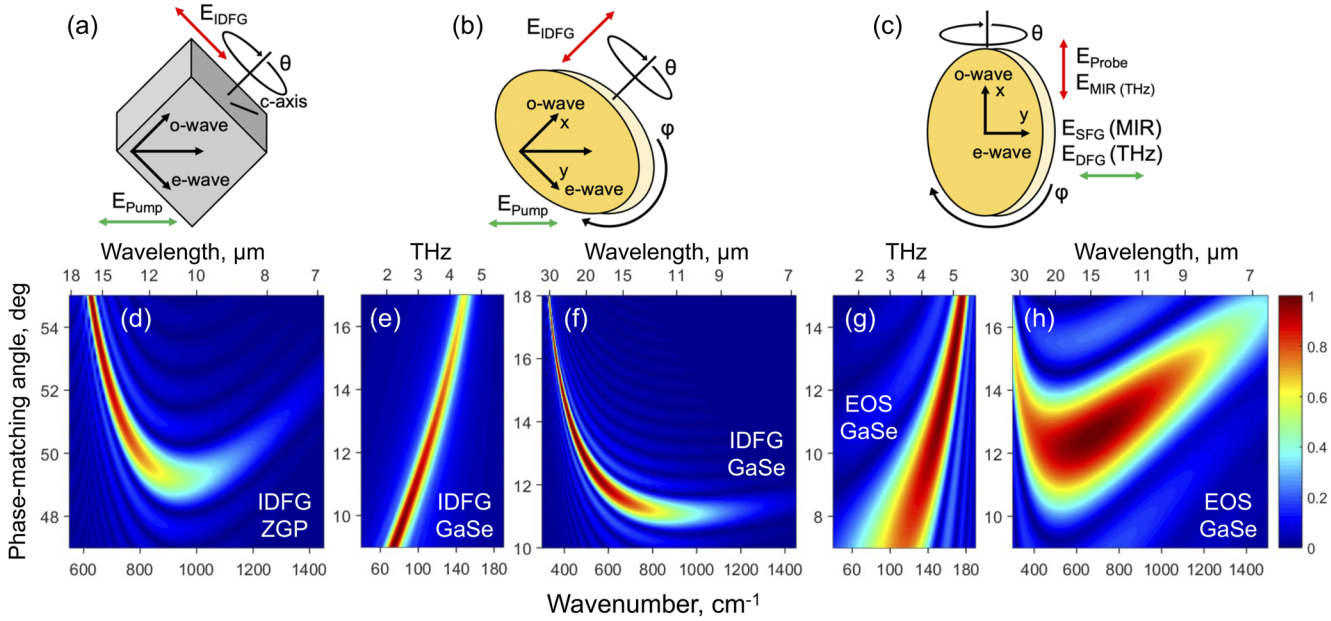

FIG. 2. (a)–(c) Orientation of nonlinear crystals relative to the polarization directions of the participating waves; (a) ZGP crystal for the type I IDFG; (b) GaSe for the type I IDFG; (c) GaSe for the type I EOS. (d-f) Color-coded 2D plots for the IDFG E-field amplitudes; (d) for MIR IDFG in a 3-mm-thick ZGP; (e) for MIR IDFG in a 1.3-mm-thick GaSe; (f) for THz IDFG in the same crystal. (g,h) Color-coded 2D plots for the normalized EOS detection efficiency for the $\lambda = 1.16$ μm probe; (g) for THz EOS in a 150-μm-thick GaSe; (h) for MIR EOS in the same crystal.

For the IDFG in GaSe, the driving laser beam was pre-chirped with a 1-mm-thick sapphire plate and focused into a 1.3-mm thick uncoated z-cut GaSe crystal using a 75-mm CaF_2 lens. We used type I phase matching ($\theta = 10–18°$, $\varphi = 90°$), corresponding to the $\omega_3^e - \omega_2^o = \omega_1^o$ process [Fig. 2(b)]. Similar to ZGP, the GaSe crystal is placed in such a way that its "*e*" and "*o*" polarization directions are at 45° with respect to that of the driving laser polarization [Fig. 2(b)], and the generated IDFG output ("o"-wave) is oriented at 45° with respect to the vertical axis of the laboratory system. With 3.15 W of driving laser power, the IDFG output power was 7 mW, with a typical spectrum shown in Fig. 3(b). Figures 2(e) and 2(f) show the color-coded plots for the normalized IDFG THz and MIR *E*-field amplitudes in GaSe. One can see that the THz output (at frequencies <200 cm^{-1}) can be generated concurrently with the MIR waves through the $\omega_3^o - \omega_2^e = \omega_1^o$ process.

C. Electro-optic sampling in the dual-comb configuration

In the electro-optic sampling (EOS) method, the electric field of the MIR/THz transient is detected via the induced change of the polarization of a NIR probe pulse inside an electro-optic (EO) crystal, where the two beams overlap. This polarization change is detected via ellipsometry using a NIR detector consisting of two balanced photodiodes. The key advantage of the DCS-EOS modality is its ultrabroadband (MIR to THz) spectral coverage without the need for cryogenically cooled photodetectors.[29,31]

For the EOS probe, we used the second harmonic (SH) of our Cr:ZnS comb No. 2. Using the SH as a probe has two benefits: (i) the SH probe pulses have a shorter duration than the fundamental ones, and (ii) one can use low-noise InGaAs balanced detectors. For SH generation, the laser output is focused into a GaSe crystal (type I phase matching, $\theta = 19.8°$; $\varphi = 90°$) using an OAP mirror (Fig. 1). The GaSe thickness (32 μm) was chosen so as to preserve the entire bandwidth of the pump laser. The SH spectrum was centered at 1.16 μm with a bandwidth of 113 nm/25 THz at FWHM and 212 nm/47 THz at −20 dB. The inset to Fig. 1 shows the normalized spectra of the fundamental (ω) laser output and its second harmonic (2ω). We did not measure the SH pulse duration, but based on the width of the spectrum, it is expected to be close to 20 fs. In addition, special care is taken to filter out, using a dichroic mirror, the SH parasitically produced in the Cr:ZnS oscillator-amplifier system. At a pump power of 2 W, the output power of the SH was 70 mW with linear polarization.

Next, both the NIR probe and MIR/THz beams are focused and spatially overlapped in a 150-μm-thick EOS z-cut GaSe crystal oriented for the type I phase-matched sum frequency (MIR + NIR) generation (SFG) process $\omega_{probe}^o + \omega_{MIR}^o = \omega_{SFG}^e$ with polar and azimuthal angles $\theta = 8–16°$ and $\varphi = 90°$ [Fig. 2(c)]. To combine the beams, we use an OAP mirror with a through hole with a diameter of 2 mm to reflect the MIR and transmit the NIR beam (Fig. 1). Since the MIR/THz beam is polarized at 45° with respect to the vertically polarized SH beam (E_{probe}), only its vertical (*o*-wave) component participates in the nonlinear interaction, while the horizontal component does not contribute to SFG. It is worth noting that despite the fact that the THz refractive index is higher than that of the optical, the EOS detection of THz transients (at < 200 cm^{-1}) is phase-matchable at the same GaSe orientation through the *difference frequency generation* (DFG) upconversion (with respect to THz) process: $\omega_{probe}^o - \omega_{THz}^o = \omega_{DFG}^e$. Figures 2(g) and 2(h) show the calculated color-coded plots for the EOS efficiency; the plot takes into account the phase-matching function $sinc(\Delta kL/2)$ and the finite spectral band of the probe pulse (long-wave absorption in the crystal is not taken into account).

Subsequently, the beam is sent to an ellipsometry setup consisting of a quarter-wave plate, a Wollaston prism, and an InGaAs balanced photodetector (BPD) from Thorlabs (model PDB450C, bandwidth 45 MHz). An attenuation filter wheel is used to keep the total power of each detector near saturation. The differential BPD signal is digitized with a 16-bit analog-to-digital converter, coherently averaged, Fourier transformed, and frequency up-scaled to obtain the MIR/THz spectrum. We use a short-pass filter (SPF, $\lambda < 1100$ nm) to improve the EOS signal-to-noise ratio (SNR) by increasing the share of the upconverted signal (that carries the spectral information) with respect to the probe.

Shown in Fig. 3(a) is the spectrum obtained with ZGP as an IDFG crystal, with two different phase-matching angles for the EOS crystal. The absorption peaks at >1300 cm^{-1} are due to water absorption in the surrounding air, and sharp peaks near 900–1000 cm^{-1} are due to the isoprene vapor present in the optical gas cell. Similarly, Fig. 3(b) shows the spectrum obtained with GaSe as an IDFG crystal, where the spectral output spans 650 cm^{-1} (9–22 μm) at a level of −40 db. The spectral feature at 667 cm^{-1} corresponds to the carbon dioxide absorption in the air. Interestingly, one can see a dip at ~510 cm^{-1} (15.3 THz) related to the lattice absorption peak in GaSe.

III. HIGH-RESOLUTION FIELD-RESOLVED DUAL COMB SPECTROSCOPY OF MOLECULES

In this section, we present our high-resolution spectroscopy study of several molecules that play an important role in exobiology and medical breath analysis. According to the DCS method, molecular vibrations are excited by few-cycle MIR/THz pulses and then coherently emit radiation that is detected by EOS. The nominal spectral sampling step in our setup is determined by the comb-mode spacing (80 MHz). However, when the absorption linewidths (predominantly Doppler-broadened in our case) are less than the mode spacing, we use the method of spectral interleaving, i.e., we combine the spectra taken with progressively shifted combs, in which case the spectral resolution can be well below the mode spacing.[28,33,34] defined in our case by the linewidth of the CW laser reference, which is <20 kHz.

To measure the molecular absorbance spectrum $A(\nu) = -\ln(I/I_0)$, where I is the light spectral intensity after it passes through the sample and I_0 is the intensity when the gas cell is evacuated, we subtract the absorbance taken with an empty cell from that taken with the cell filled with a sample gas. This allows for obtaining an accurate baseline and, in addition, for eliminating parasitic Fabry–Perot oscillations from parallel surfaces.

A. Mixture of CO_2 and C_2H_2

Figure 4 shows a high-resolution EOS-DCS absorption spectrum of a low-pressure mixture of carbon dioxide (CO_2) and

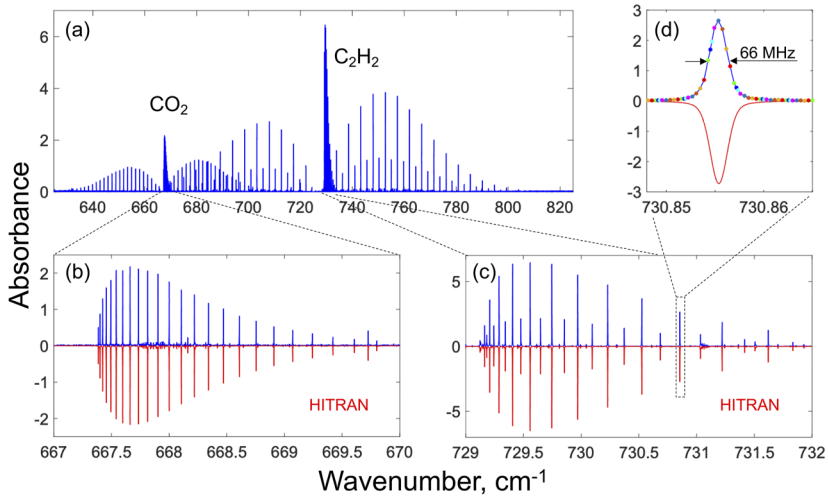

FIG. 4. (a) High-resolution spectrum of a mixture of CO_2 and C_2H_2 molecules with N_2 as a buffer gas at 4 mbar pressure. (b) Expanded view of the CO_2 spectrum and its comparison with the HITRAN simulation. (c) Expanded view of the C_2H_2 (acetylene) spectrum and its comparison with HITRAN. (d) Zoomed-in absorption line of C_2H_2 showing how spectral data points of shifted combs were combined into one spectrum.

acetylene (C_2H_2). The two frequency combs had a repetition frequency offset of Δf_{rep} = 91 Hz. A 20 cm-long absorption cell with AR coated (7–12 μm) Ge windows was filled with the gas mixture with the concentrations for each molecule at around 1% in N_2 buffer gas at 4 mbar total pressure. As a sensing comb, we used the IDFG output produced in GaSe with a spectrum similar to the one shown in Fig. 3(b). The absorbance spectra shown in Fig. 4 are combined from 8 interleaved comb-mode-resolved spectra to create a high-resolution spectrum with an average spacing of 10 MHz, which allows for fully resolving the narrow (66 MHz) absorption features. The expanded images of individual CO_2 and C_2H_2 spectra and their comparison with the HITRAN simulation (shown as inverted peaks) are shown in Figs. 4(b) and 4(c), respectively. Spectral points of varying colors in Fig. 4(d) illustrate how the spectra from the shifted combs were combined together. For each comb-mode-resolved spectrum, a single waveform was coherently averaged, and with the number of averages at 100 000, it took 18 min per measurement.

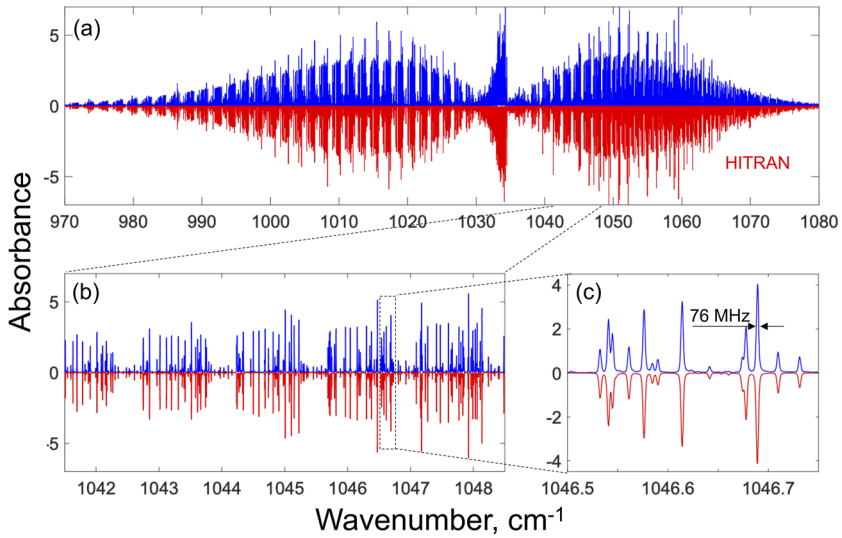

FIG. 5. (a) High-resolution spectrum of methanol at 0.81 mbar pressure. (b) and (c) Zoomed-in portions of the spectrum. The simulated (HITRAN) spectrum is shown in red and inverted for clarity.

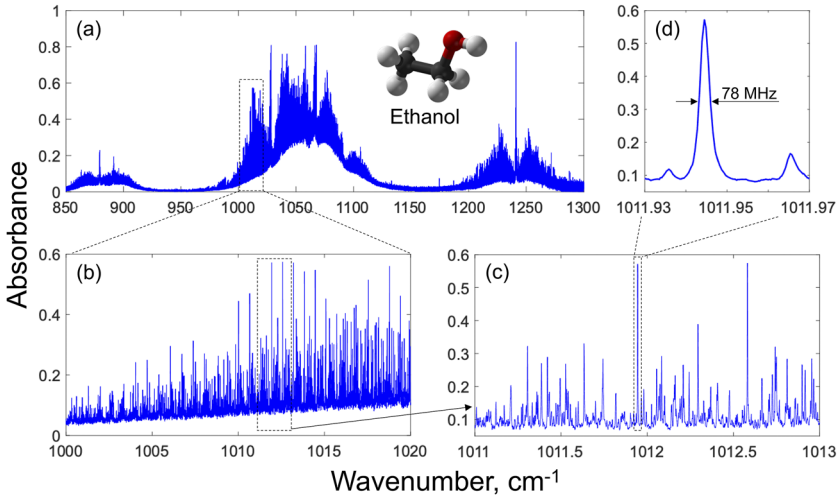

FIG. 6. High-resolution spectrum of ethanol at 2 mbar pressure. (b)–(d) Zoomed-in portions of the spectrum.

B. Methanol

Figure 5 shows the high-resolution spectrum of methanol with a predominantly Doppler-broadened linewidth (76 MHz). In this and subsequent experiments, the two combs were operated with a repetition frequency offset of Δf_{rep} = 69 Hz. A 45 cm-long absorption cell with Ge windows was filled with methanol vapor at 0.81 mbar pressure. As the sensing comb, we used the IDFG output from ZGP. The absorption spectrum here is a combination of 11 interleaved comb-mode resolved spectra. The simulated (HITRAN) spectrum is shown in red and inverted. In this experiment, we coherently averaged 50 000 waveforms, which took 12 minutes per comb-mode-resolved spectrum.

It can be seen from Figs. 4 and 5 that there is excellent agreement with the HITRAN simulation for CO_2, C_2H_2, and methanol in terms of line positions, line widths, and line strengths.

C. Ethanol, isoprene, and dimethyl sulfide (DMS)

Figures 6–8 show high-resolution vapor spectra of ethanol, isoprene, and dimethyl sulfide obtained at low pressures with the sensing comb produced via IDFG in ZGP. We employed a 45-cm-long absorption gas cell with Ge windows; the vapor pressures of ethanol, isoprene, and dimethyl sulfide were set at 2.0, 4.0, and 13 mbar, respectively. We obtained 6 interleaved spectra for ethanol

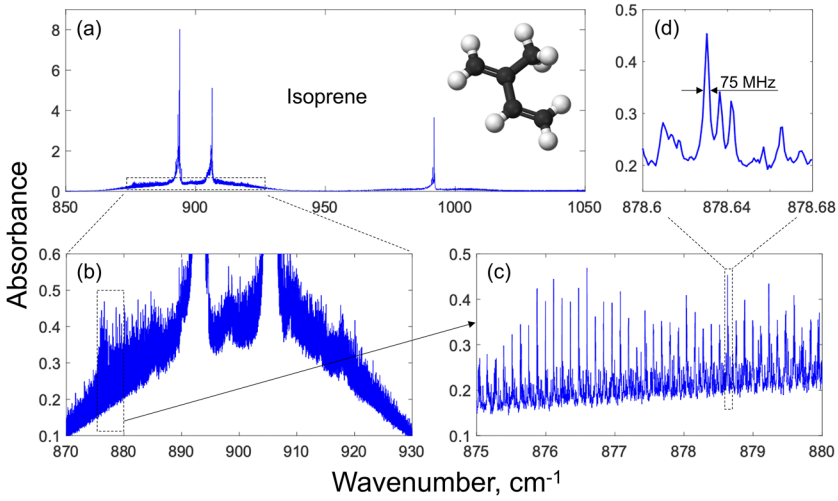

FIG. 7. High-resolution spectrum of isoprene at 4 mbar pressure. (b)–(d) Zoomed-in portions of the spectrum.

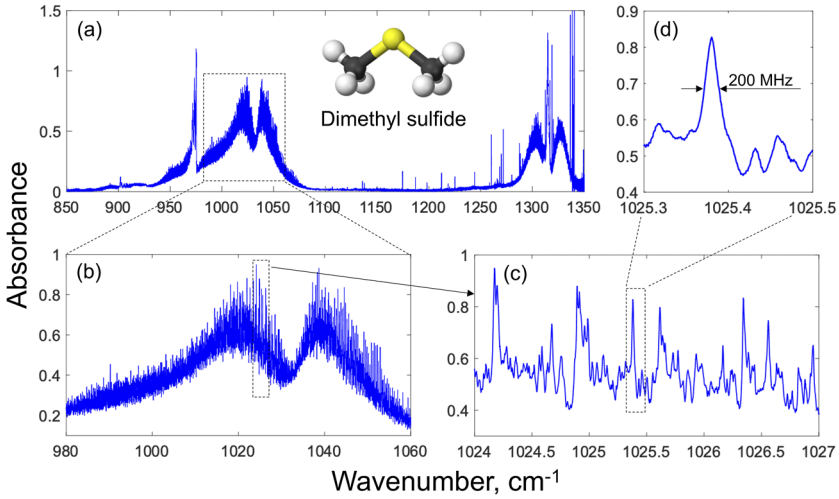

FIG. 8. High-resolution spectrum of DMS at 13 mbar pressure. (b)–(d) Zoomed-in portions of the spectrum.

(Fig. 6), 3 for isoprene (Fig. 7), and 3 for dimethyl sulfide (Fig. 8), such that the data point spacing varied between 13 and 26 MHz. The number of averages was 100 000 per waveform, which took 24 minutes for each comb-mode-resolved spectrum.

We emphasize that the fine spectroscopic features of these three molecules have remained unexplored until now. A separate work will be dedicated to their spectroscopic study involving in-depth analysis and the creation of the line lists for the databases.

IV. MEASUREMENTS AT A VIDEO RATE

Thanks to the high SNR of our DCS-EOS system, we explored the possibility of performing broadband comb-mode-resolved spectroscopy at high speed. As the sensing comb, we used the IDFG output produced in ZGP, consisting of ~200 000 comb modes with a comb center frequency of around 1000 cm^{-1} and a width of 530 cm^{-1} at a level of −20 dB. A 45-cm-long optical gas cell was filled with methanol vapor at a partial pressure of 1 mbar and diluted in air at a total pressure of 20 mbar. Figure 9 shows a portion of the spectrum at different acquisition times. Even at 14.5-ms acquisition time (69 Hz rate, single waveform), we were able to detect the fine structure of methanol with a signal-to-noise ratio of 22. We did not use the time-domain apodization; hence, the spectral resolution corresponding to the comb-mode spacing of 80-MHz was preserved.

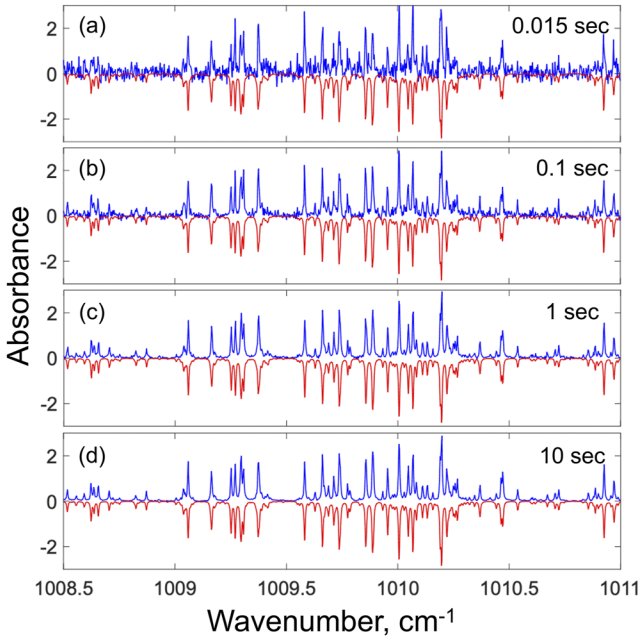

FIG. 9. Portion of the absorption spectrum of methanol at a buffer gas (air) pressure of 20 mbar corresponding to different averaging times ranging from 14.5 ms (single waveform) to 10 s (687 averages).

V. SPECTROSCOPY AT TERAHERTS FREQUENCIES

Figure 10(a) shows the longwave portion of the spectrum obtained with a 1.3-mm-thick IDFG GaSe crystal in combination with a 150-μm-thick EOS GaSe with the optical gas cell removed. The spectrum was obtained in two measurements, each with different phase-matching angles of the IDFG and EOS crystals. The spectrum is modulated by strong absorption lines in the surrounding atmosphere. Figure 10(b) displays the absorbance spectrum $A(\nu)$, derived from window 1 of Fig. 10(a), in the region 85-130 cm^{-1} (2.55–3.9 THz). The spectrum, consisting mostly of water absorption lines, is compared with the HITRAN simulation (displayed in red and inverted). Similarly, we derived the absorbance spectrum from window 2 in the region 350–400 cm^{-1} (10.5–12 THz) that is shown in Fig. 10(c) and compared it with the HITRAN simulation. We observed good agreement between the measured and simulated peaks, with the exception of some high absorption peaks

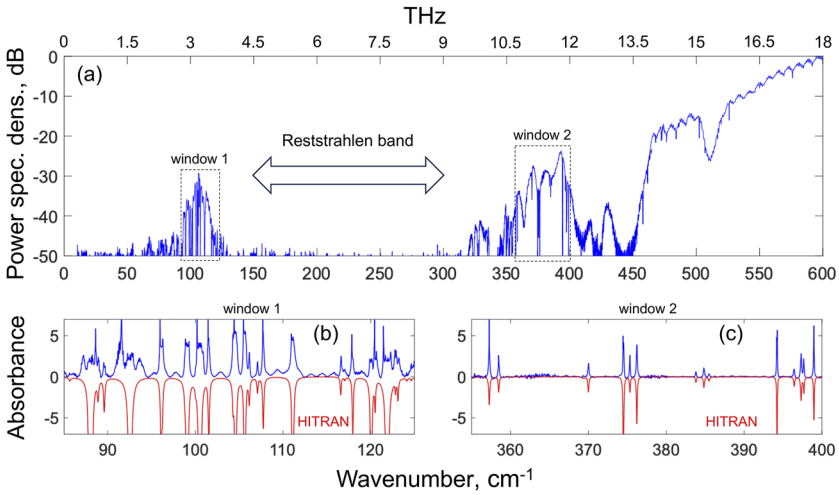

FIG. 10. (a) Longwave IDFG spectrum that features atmospheric absorption at 50–500 cm^{-1} (1.5–15 THz). A dip at 340 cm^{-1} is due to the absorption in the Ge substrate of the long-pass filter used. (b) Absorbance spectrum derived from Window 1 of the emission spectrum. (c) Absorbance spectrum derived from Window 2. The simulated (HITRAN) absorbance spectra for the ambient air are shown in red and inverted for clarity.

whose shapes were not resolved due to the limited dynamic range. Between windows 1 and 2, there is a highly absorbing Reststrahlen band of GaSe at about 4.5–9 THz, corresponding to strong lattice resonances.

VI. DETECTION LIMITS AND THE FIGURE OF MERIT

In the time domain, our EOS-DCS signal exhibits an SNR of typically 1.2×10^3 for a single (no averaging) waveform (we define SNR as a ratio of the peak signal to its standard deviation at the end of the waveform, where we assume the molecular free induction decay fades out). This SNR is dominated by the shot noise of the NIR balanced photodetector (BPD); in fact, when operating near the BPD saturation power of 1.5 mW for each channel (1 mA current per diode, I = 2 mA total), we find that for the peak differential current ΔI = 0.2 mA (so that $\Delta I/I$ = 10%) observed with the transients from ZGP crystal with the spectrum of Fig. 3(a) and for the 45-MHz detection bandwidth, the shot noise-limited SNR closely matches our experimental value. The measured differential photocurrent corresponds to an upconversion efficiency of the probe to the sum frequency of 2.6%. Upconversion of the NIR probe inside the EOS crystal occurs due to interaction with the MIR field. Despite the fact that the size of the MIR beam (60 μm) is larger than that of the probe (20 μm), it is not a bottleneck since the SNR is dominated by the shot noise of the BPD; also, the differential photocurrent $\Delta I/I$ cannot be increased significantly above 10% as this will degrade the field detection linearity.[35] With coherent averaging of the waveforms, the SNR scales as the square root of the averaging time (τ), as verified in our experiments with up to 10^6 averages (242 min at Δf_{rep} = 91 Hz). (For each waveform, the data acquisition process is triggered by its sharp rising edge, which can be regarded as a long-term phase drift correction as it compensates for possible time jitter between waveforms.[11,28] This explains the fact that the averaging time can be much longer than the mutual coherence time, 100 s in our case, between the two combs.) With this number of averages, the time-domain dynamic range is ~10^6 for field detection and ~10^{12} for intensity, which corresponds to the capability of detecting MIR fields of ~0.6 V/cm inside the EOS crystal.

In the frequency domain, the spectral noise is characterized by the fractional standard deviation of the spectral power density I_s ($\sigma_S = \Delta I_s/I_s$). We find that the spectral SNR = $1/\sigma_S$ scales as $\sqrt{\tau}$, such that SNR/$\sqrt{\tau}$ = 62 $Hz^{1/2}$ near the comb maximum; this value exceeds the value of 36 $Hz^{1/2}$ obtained in the DCS system[28] under similar comb generation conditions and comb width (IDFG comb produced in ZGP crystal), but using a HgCdTe detector. This provides a strong argument in favor of the EOS-DCS mode, especially when operating beyond the 12 μm wavelength. For the number of modes M ≈ 62 000 within the central (at half-maximum) portion of the comb of Fig. 3(a), this gives the DCS figure of merit (defined in Ref. 2) of M × SNR/$\sqrt{\tau}$ = 3.8×10^6 $Hz^{1/2}$.

VII. CONCLUSION

Using an EOS-DCS approach, we performed high-resolution spectroscopic measurements across an ultra-broadband, 1.5 to 45 THz (6.6–200 μm), longwave frequency range (except for the Reststrahlen band, 4.5–9 THz) with the acquisition of octave-wide MIR spectra containing 200 000 comb-mode resolved lines at a video rate (69 Hz). This result was facilitated by using 2.35-μm mode-locked Cr:ZnS lasers as the front end, with the benefits of low noise and the ability to provide high IDFG conversion efficiency. With the nominal spectral resolution given by the comb-mode spacing (80 MHz), we were able to perform measurements with better than 10 MHz resolution via spectral interleaving. The ability to simultaneously perform high-resolution spectroscopic measurements in the MIR and THz ranges will make it possible to relate different molecular motions, for example, vibrational and librational. This new method also paves the way for creating highly accurate molecular

spectroscopic databases and has the potential for real-time medical diagnostics through multi-species exhaled breath analysis. Our next step will be compressing the driving laser pulses to sub-10 fs duration, allowing for extending the spectral coverage from 1 to 100 THz (3–300 μm).

ACKNOWLEDGMENTS

We acknowledge support from the Defense Advanced Research Projects Agency (DARPA), Grant No. W31P4Q-15-1-0008; from the Office of Naval Research (ONR), Grant Nos. N00014-15-1-2659, N00014-18-1-2176, N00014-17-1-2705, and N68335-20-C-0251; from the Department of Energy (DOE), Grant No. B&R #KA2601020; and from the US Air Force Office of Scientific Research (AFOSR), Grant No. FA9550-23-1-0126.

AUTHOR DECLARATIONS

Conflict of Interest

The authors have no conflicts to disclose.

Author Contributions

Dmitrii Konnov: Investigation (equal); Methodology (equal); Writing – original draft (equal). **Andrey Muraviev**: Methodology (equal); Project administration (equal); Resources (equal); Writing – review & editing (equal). **Sergey Vasilyev**: Conceptualization (equal); Methodology (equal); Resources (equal). **Konstantin Vodopyanov**: Conceptualization (equal); Formal analysis (equal); Writing – original draft (equal).

DATA AVAILABILITY

The data that support the findings of this study are available from the corresponding author upon reasonable request.

REFERENCES

[1]N. Picqué and T. W. Hänsch, "Frequency comb spectroscopy," Nat. Photonics **13**, 146–157 (2019).
[2]I. Coddington, N. Newbury, and W. Swann, "Dual-comb spectroscopy," Optica **3**, 414–426 (2016).
[3]F. Keilmann, C. Gohle, and R. Holzwarth, "Time-domain mid-infrared frequency-comb spectrometer," Opt. Lett. **29**, 1542–1544 (2004).
[4]M. E. Fermann and I. Hartl, "Ultrafast fibre lasers," Nat. Photonics **7**, 868–874 (2013).
[5]S. B. Mirov, I. S. Moskalev, S. Vasilyev, V. Smolski, V. V. Fedorov, D. Martyshkin, J. Peppers, M. Mirov, A. Dergachev, and V. Gapontsev, "Frontiers of MIR lasers based on transition metal doped chalcogenides," IEEE J. Sel. Top. Quantum Electron. **24**, 1601829 (2018).
[6]S. Vasilyev, V. Smolski, J. Peppers, I. Moskalev, M. Mirov, Y. Barnakov, S. Mirov, and V. Gapontsev, "Middle-IR frequency comb based on Cr:ZnS laser," Opt. Express **27**, 35079–35087 (2019).
[7]S. Vasilyev, I. Moskalev, V. Smolski, J. Peppers, M. Mirov, Y. Barnakov, V. Fedorov, D. Martyshkin, S. Mirov, and V. Gapontsev, "Kerr-lens mode-locked Cr:ZnS oscillator reaches the spectral span of an optical octave," Opt. Express **29**, 2458–2465 (2021).
[8]S. Qu, A. Paudel, A. Sebesta, P. Steinleitner, N. Nagl, M. Poetzlberger, V. Pervak, K. F. Mak, and A. Weigel, "Directly diode-pumped femtosecond Cr:ZnS amplifier with ultra-low intensity noise," Opt. Lett. **47**, 6217 (2022).
[9]F. Adler, K. C. Cossel, M. J. Thorpe, I. Hartl, M. E. Fermann, and J. Ye, "Phase-stabilized, 1.5 W frequency comb at 2.8–4.8 μm," Opt. Lett. **34**, 1330–1332 (2009).
[10]O. Kara, L. Maidment, T. Gardiner, P. G. Schunemann, and D. T. Reid, "Dual-comb spectroscopy in the spectral fingerprint region using OPGaP optical parametric oscillators," Opt. Express **25**, 32713 (2017).
[11]A. V. Muraviev, V. O. Smolski, Z. E. Loparo, and K. L. Vodopyanov, "Massively parallel sensing of trace molecules and their isotopologues with broadband subharmonic mid-infrared frequency combs," Nat. Photonics **12**, 209–214 (2018).
[12]Q. Ru, T. Kawamori, P. G. Schunemann, S. Vasilyev, S. B. Mirov, and K. L. Vodopyanov, "Two-octave-wide (3–12 μm) subharmonic produced in a minimally dispersive optical parametric oscillator cavity," Opt. Lett. **46**, 709–712 (2021).
[13]G. Ycas, F. R. Giorgetta, E. Baumann, I. Coddington, D. Herman, S. A. Diddams, and N. R. Newbury, "High-coherence mid-infrared dual-comb spectroscopy spanning 2.6 to 5.2 μm," Nat. Photonics **12**, 202–208 (2018).
[14]M. Yan, P.-L. Luo, K. Iwakuni, G. Millot, T. W. Hänsch, and N. Picqué, "Mid-infrared dual-comb spectroscopy with electro-optic modulators," Light: Sci. Appl. **6**, e17076 (2017).
[15]H. Timmers, A. Kowligy, A. Lind, F. C. Cruz, N. Nader, M. Silfies, G. Ycas, T. K. Allison, P. G. Schunemann, S. B. Papp, and S. A. Diddams, "Molecular fingerprinting with bright, broadband infrared frequency combs," Optica **5**, 727–732 (2018).
[16]S. Vasilyev, I. S. Moskalev, V. O. Smolski, J. M. Peppers, M. Mirov, A. V. Muraviev, K. Zawilski, P. G. Schunemann, S. B. Mirov, K. L. Vodopyanov, and V. P. Gapontsev, "Super-octave longwave mid-infrared coherent transients produced by optical rectification of few-cycle 2.5-μm pulses," Optica **6**, 111–114 (2019).
[17]P. G. Schunemann, K. T. Zawilski, L. A. Pomeranz, D. J. Creeden, and P. A. Budni, "Advances in nonlinear optical crystals for mid-infrared coherent sources," J. Opt. Soc. Am. B **33**, D36–D43 (2016).
[18]V. Petrov, "Frequency down-conversion of solid-state laser sources to the mid-infrared spectral range using non-oxide nonlinear crystals," Prog. Quantum Electron. **42**, 1–106 (2015).
[19]K. L. Vodopyanov, *Laser-based Mid-infrared Sources and Applications* (Wiley, 2020).
[20]A. L. Gaeta, M. Lipson, and T. J. Kippenberg, "Photonic-chip-based frequency combs," Nat. Photonics **13**, 158–169 (2019).
[21]L. Chang, S. Liu, and J. E. Bowers, "Integrated optical frequency comb technologies," Nat. Photonics **16**(2), 95–108 (2022).
[22]K. Luke, Y. Okawachi, M. R. E. Lamont, A. L. Gaeta, and M. Lipson, "Broadband mid-infrared frequency comb generation in a Si_3N_4 microresonator," Opt. Lett. **40**, 4823–4826 (2015).
[23]B. Kuyken, T. Ideguchi, S. Holzner, M. Yan, T. W. Hänsch, J. Van Campenhout, P. Verheyen, S. Coen, F. Leo, R. Baets, G. Roelkens, and N. Picqué, "An octave-spanning mid-infrared frequency comb generated in a silicon nanophotonic wire waveguide," Nat. Commun. **6**(1), 6310 (2015).
[24]A. Hugi, G. Villares, S. Blaser, H. C. Liu, and J. Faist, "Mid-infrared frequency comb based on a quantum cascade laser," Nature **492**, 229–233 (2012).
[25]M. Lepère, O. Browet, J. Clément, B. Vispoel, P. Allmendinger, J. Hayden, F. Eigenmann, A. Hugi, and M. Mangold, "A mid-infrared dual-comb spectrometer in step-sweep mode for high-resolution molecular spectroscopy," J. Quant. Spectrosc. Radiat. Transfer **287**, 108239 (2022).
[26]J. A. Agner, S. Albert, P. Allmendinger, U. Hollenstein, A. Hugi, P. Jouy, K. Keppler, M. Mangold, F. Merkt, and M. Quack, "High- resolution spectroscopic measurements of cold samples in supersonic beams using a QCL dual-comb spectrometer," Mol. Phys.**120**, e2094297 (2022).
[27]M. Bagheri, C. Frez, L. A. Sterczewski, I. Gruidin, M. Fradet, I. Vurgaftman, C. L. Canedy, W. W. Bewley, C. D. Merritt, C. S. Kim, M. Kim, and J. R. Meyer, "Passively mode-locked interband cascade optical frequency combs," Sci. Rep. **8**, 3322 (2018).
[28]S. Vasilyev, A. Muraviev, D. Konnov, M. Mirov, V. Smolski, I. Moskalev, S. Mirov, and K. L. Vodopyanov, "Longwave infrared (6.6–11.4 μm) dual-comb

spectroscopy with 240,000 comb-mode-resolved data points at video rate," Opt. Lett. **48**, 2273 (2023).
[29]A. S. Kowligy, H. Timmers, A. J. Lind, U. Elu, F. C. Cruz, P. G. Schunemann, J. Biegert, and S. A. Diddams, "Infrared electric field sampled frequency comb spectroscopy," Sci. Adv. **5**, eaaw8794 (2019).
[30]Q. Wu and X.-C. Zhang, "Free-space electro-optic sampling of terahertz beams," Appl. Phys. Lett. **67**, 3523–3525 (1995).
[31]A. Sell, R. Scheu, A. Leitenstorfer, and R. Huber, "Field-resolved detection of phase-locked infrared transients from a compact Er:fiber system tunable between 55 and 107 THz," Appl. Phys. Lett. **93**, 251107 (2008).
[32]I. Pupeza, M. Huber, M. Trubetskov, W. Schweinberger, S. A. Hussain, C. Hofer, K. Fritsch, M. Poetzlberger, L. Vamos, E. Fill, T. Amotchkina, K. V. Kepesidis, A. Apolonski, N. Karpowicz, V. Pervak, O. Pronin, F. Fleischmann, A. Azzeer, M. Žigman, and F. Krausz, "Field-resolved infrared spectroscopy of biological systems," Nature **577**, 52 (2020).
[33]Y.-D. Hsieh, Y. Iyonaga, Y. Sakaguchi, S. Yokoyama, H. Inaba, K. Minoshima, F. Hindle, T. Araki, and T. Yasui, "Spectrally interleaved, comb-mode-resolved spectroscopy using swept dual terahertz combs," Sci. Rep. **4**, 3816 (2014).
[34]A. V. Muraviev, D. Konnov, and K. L. Vodopyanov, "Broadband high-resolution molecular spectroscopy with interleaved mid-infrared frequency combs," Sci. Rep. **10**, 18700 (2020).
[35]C. Riek, D. V. Seletskiy, and A. Leitenstorfer, "Femtosecond measurements of electric fields: From classical amplitudes to quantum fluctuations," Eur. J. Phys. **38**, 024003 (2017).